Electronic Supplementary Information

Stabilizing Nickel-Rich Layered Oxide Cathodes by Magnesium Doping for Rechargeable Lithium-ion Batteries

Hang Li,[a] Pengfei Zhou,[a,b] Fangming Liu,[a] Haixia Li,[a] Fangyi Cheng*[a], and Jun Chen[a]

[a]Key Laboratory of Advanced Energy Materials Chemistry (Ministry of Education), College of Chemistry, Nankai University, Tianjin 300071, China.
Email: fycheng@nankai.edu.cn
[b]School of Chemistry and Chemical Engineering, Shandong University of Technology, Zibo 255049, China

Experimental Section

Synthesis of $LiNi_{0.9}Co_{0.07}Mg_{0.03}O_2$

$LiNi_{0.9}Co_{0.07}Mg_{0.03}O_2$ microspheres were synthesized by a two-step route involving coprecipitation and calcination. In a typical synthesis, three solutions were firstly prepared: solution A, a mix of $NiSO_4$•$6H_2O$ (0.9 M), $CoSO_4$•$7H_2O$ (0.07 M), and $MgSO_4$ (0.03 M) in distilled water; solution B, an aqueous mix of NaOH (1.0 M) and NH_4OH (1.0 M); solution C, aqueous 3.0 M NaOH. Under air atmosphere, 200 mL distilled water was added in a continuous stirred tank reactor (CSTR), which was maintained at 50 ^oC. After adjusting the pH to 10.7 with 2 mL NH_4OH and adequate solution C, equivalent amount of solution A and solution B were simultaneously pumped into the CSTR. The pH of the mixed solution in the CSTR was fixed at 10.7 ± 0.2 using solution C. The stirring speed, temperature, and solution pH in the CSTR were controlled strictly. Then, the formed greenish $Ni_{0.9}Co_{0.07}Mg_{0.03}(OH)_2$ precursor was filtered and washed repeatedly with deionized water until the pH of the filtrate was close to 7.0. The filtered powders were dried at 120 ^oC for 10 h. Finally, the $Ni_{0.9}Co_{0.07}Mg_{0.03}(OH)_2$ precursor was thoroughly mixed with $LiOH$•H_2O (molar ratio 1:1.02) and calcinated at 550 ^oC for 6 h, followed by heating at 700 ^oC for 12 h under oxygen gas flowing. The benchmark NCM811 powders were provided by Kejing Star Technology Shenzhen.

Characterization Methods

The morphology and phase of the prepared $Ni_{0.9}Co_{0.07}Mg_{0.03}(OH)_2$ precursor and $LiNi_{0.9}Co_{0.07}Mg_{0.03}O_2$ were characterized by field-emission scanning electron microscopy (SEM,

JEOL JSM7500F) equipped with energy dispersive spectroscopy (EDS), field-emission transmission electron microscopy (TEM, Philips Tecnai-F20), and powder X-ray diffraction (XRD, Rigaku SmartLab, Cu Kα radiation). Annular bright-field (ABF) and high-angel annular dark-field (HAADF) images were obtained with a cold field-emission gun and double-hexapole Cs correctors (CEOS GmbH, Heidelberg, Germany) equipped on a scanning TEM microscope (JEOL JEM-ARM200CF) with operating voltage of 200 kV. The chemical compositions of samples were measured by inductive coupled plasma atomic emission spectrometry (ICP-AES, PerkinElmer Optima 8300). Specific surface area was determined by N_2 adsorption on a BELSORP-mini instrument. The particle size distribution was measured by laser particle size analyzer (Mastersizer S). Spherical particles were incised to obtain the cross-section area information by focused ion beam (Helios NanoLab 460HP). *In-situ* XRD analysis was carried on by a modified CR2032 coin cell. The positive shell was punched to acquire an 8-mm hole, which was sealed with an ultrathin aluminum foil as the window for X-ray entrance. The *in-situ* cells were charged at 0.2 C rate and XRD data points were recorded at a scan speed of 20^{o} min^{-1}. The thermal stability of the cathode materials at charged voltages of 4.3, 4.5, and 4.7 V was examined with a differential scanning calorimetry (DSC, Netzsch STA 449F3) from 30 to 350 ℃ at a heating rate of 10 ℃ min^{-1}. To estimate the amount of residual surface alkali, we applied a two-step titration method. The sample with residual surface alkali species (LiOH and Li_2CO_3) were first dissolved in water and filtrated. The filtrate was titrated with pre-calibrated dilute HCl sequentially using phenolphthalein and methyl red indicator, based on the following equations:

First titration: $Li_2CO_3 + HCl = LiCl + LiHCO_3$; $LiOH + HCl = LiCl + H_2O$

Second titration: $LiHCO_3 + HCl = LiCl + H_2CO_3$; $H_2CO_3 = H_2O + CO_2\uparrow$

Electrochemical Measurements

CR2032 coin-type cells were used for electrochemical tests. The cathode was prepared by blending the oxide sample, Super P, and poly(vinylidenefloride) with a weight ratio of 85:7.5:7.5 in N-methyl-2-pyrrolidone. The slurry was painted onto an aluminum foil and vacuum-dried at 120 ^{o}C

for 12 h. The electrode was cut into pellets with a diameter of 10 mm (active mass ~5 mg) and pressed under 5 MPa for 5 s. Metallic lithium was used as the anode and reference electrode. Polypropylene membrane (Celgard 2400) was used as the separator. The electrolyte comprised 1.15 M $LiPF_6$ in a 1:2:2 (volume) mixture of ethylene carbonate, dimethyl carbonate, and ethyl methyl carbonate. The cells were assembled in an argon-filled glove box (Mikrouna Universal 2440/750) with H_2O and O_2 concentration below 1 ppm. To assemble full cells, the graphite anode was employed and the active mass ratio of cathode to anode was 1.7:1. Voltammetry was performed on a CHI600D Electrochemical Workbench. The cells were galvanostatically cycled on a LAND-CT2001A battery-testing system at different rates (1 C equals to 180 mA g^{-1}). The ending discharge voltage was fixed at 2.8 V and the cut-off charge voltage was separately set at 4.3, 4.5, and 4.7 V. Electrochemical impedance spectroscopy (EIS) was carried out on Parstat 2273 electrochemical workstation with an amplitude of 10 mV in the frequency ranging from 100 kHz to 5 mHz. The galvanostatic intermittent titration technique (GITT) measurement was programmed by applying a constant current of 0.1 C for 10 min and subsequently relaxing for 40 min between 2.8 and 4.5 V. Unless stated, all electrochemical data were collected at 25 ^{o}C with reported potentials versus Li^+/Li.

XRD Rietveld refinement

The refined XRD patterns of samples were calculated by Rietveld method using Fullprof program based on the hexagonal structure, R-3m space group. Normally, the Li ions occupy 3a (0, 0, 0) sites, Ni ions occupy 3b (0, 0, 0.5) sites, and O ions locate in 6c (0, 0, 0.25) sites. Herein, we suppose that Ni^{2+} and Mg^{2+} ions at 3b sites could be exchanged with Li^+ ions at 3a sites due to the similarity of their ionic radii (Ni^{2+}, 0.69 Å; Mg^{2+}, 0.72 Å; Li^+, 0.76 Å).[1] For Co^{3+} (0.545 Å), the ionic radii is much smaller than that of Li^+, so the possibility of Co^{3+} incorporation into Li layers is eliminated in the refinement. Thus, the chemical formula can be written as $(Li_1Ni_1Mg_1)_{3a}(Li_2Ni_2Mg_2Co)_{3b}O_2$. We have also considered that Mg only locates at either 3a or 3b sites alone, but some of the refined

results show wrong physical meanings and the calculated molar ratios are not in good agreement with ICP results.

ABF and HAADF Imaging

The annular bright field (ABF) images are acquired by using an annular detector spanning a range in the illumination cone of the focused electron beam. High-angle annular dark-field (HAADF) images are recorded by collecting high angle, incoherently scattered electrons with an annular dark-field detector. Contrast of the images correlates with the atomic number (Z) at definite fixed probe and detector factors, roughly following a $Z^{1/3}$ and $Z^{1.7}$ dependence for ABF and HAADF, respectively.[2] Compared with the $Z^{1.7}$ ordering in HAADF, the relatively weak Z dependence in ABF makes it possible to discriminate light and heavy atom columns simultaneously. Previous studies have shown the identification of Li, O and 3d transition metal columns in oxide electrode materials.[3-5]

GITT measurements and the calculation of the diffusion coefficient

Before the GITT measurement, the cells were first cycled at 0.1 C rate in voltage range of 2.8–4.5 V for two cycles to stabilize the batteries. Then, the cells were charged for 10 min, followed by a relaxation interval of 40 min to make the voltage reach the equilibrium. These procedures were repeatedly applied to the cells during the entire charge/discharge process. The D_{Li^+} can be calculated by Equation (S1):[6]

$$D_{Li^+}=\frac{4}{\pi}\left(\frac{m_B V_M}{M_B A}\right)^2\left(\frac{\Delta E_S}{\tau(dE_\tau/d\sqrt{\tau})}\right)^2 \qquad (\tau \ll L^2/D_{Li^+}) \qquad (S1)$$

where m_B and M_B are the mass and molecular weight (g mol^{-1}) of the cathode material respectively, and τ is the relaxation time. Molar volume V_m (cm^3 mol^{-1}) is calculated from the crystal structure data and equals to $(N_A \times V_{unit})/3$, where N_A is Avogadro constant, and V_{unit} is the volume of the unit cell. A is the total contact area between the cathode material and electrolyte. L is the average thickness of the electrode. ΔE_S is the difference in the open circuit voltage measured at the end of the relaxation period for two successive steps. $dE_\tau/d\sqrt{\tau}$ is the slope of the linearized region of the

potential E_τ during the current pulse of duration time τ. When the cell voltage during titration is linearly proportional to $\tau^{1/2}$, Equation (S1) can be further simplified as Equation (S2).[6]

$$D_{Li^+}=\frac{4}{\pi\tau}\left(\frac{m_B V_M}{M_B A}\right)^2\left(\frac{\Delta E_S}{\Delta E_\tau}\right)^2 \quad (S2)$$

Assembly of LIBs full cells

The conductive graphite (KS_6) anodes were prepared by blending 90 wt% KS_6 active material and 10 wt% PVdF binder in N-methyl-2-pyrrolidone. The obtained slurry was pasted onto copper foil and dried at 80 ^oC for 12 h in vacuum. Then, the anodes were cut into pellets with the diameter of 12 mm and were pressed at 10 MPa for 5 s. For full cell demonstration, the composite anodes were precycled in half cells between 0.01 and 1.0 V and the cells were disassembled at charged state, then reassembled with fresh $LiNi_{0.9}Co_{0.07}Mg_{0.03}O_2$ cathodes into full cells. The active material weight ratio of $LiNi_{0.9}Co_{0.07}Mg_{0.03}O_2$ to graphite is about ~1.7.

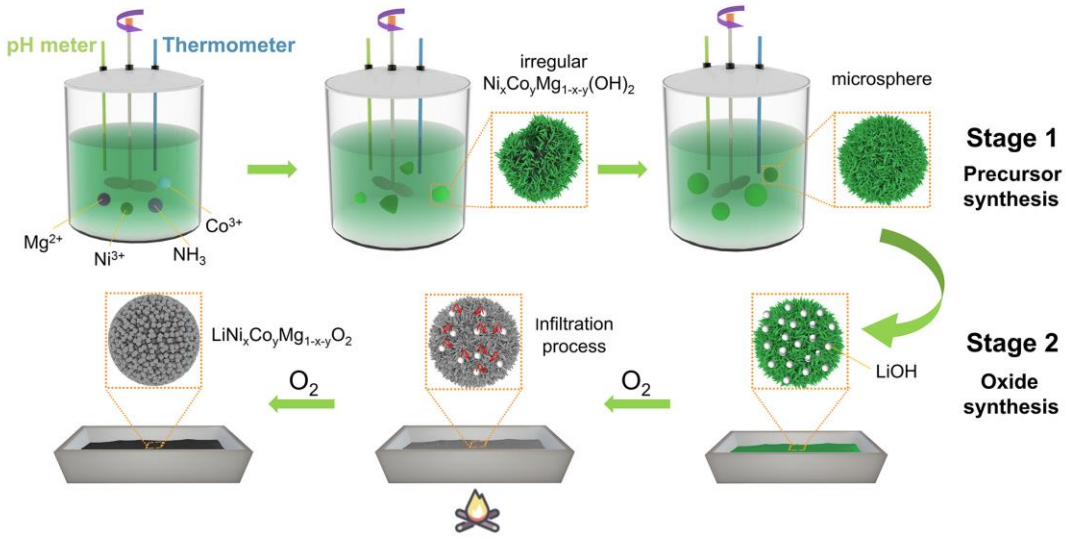

Figure S1. Schematic illustration of the synthesis of $LiNi_xCo_yMg_{1-x-y}O_2$ (NCMg) microspheres via co-precipitation and subsequent calcination.

The diagram displays a two-step preparation process. In the first step to obtain hydroxide precursor, Mg^{2+}, Ni^{2+} and Co^{2+} co-precipitate with the assistance of ammonia complexation. The pH value and ammonia concentration in the continuous stirred tank reactor (CSTR) are key factors for

the formation of uniform ternary hydroxide precursors. In the ceramic lithiation process, the hydroxide precursor reacts with LiOH in O_2 to form NCMg. The calcination temperature plays an important role in affecting the crystallinity, grain size and morphology of the obtained oxides.

Table S1. Synthetic conditions and chemical composition analysis of NCMgOH precursor series determined by ICP-AES.

Sample	pH	c(NH_4OH)	Metal Molar ratio (%)		
			Ni	Co	Mg
NCMgOH1	10.5	0.3 M	0.8742	0.0687	0.0571
NCMgOH2	10.7	0.3 M	0.8984	0.0682	0.0324
NCMgOH3	11.0	0.3 M	0.8991	0.0694	0.0315
NCMgOH4	10.7	0.7 M	0.8990	0.0692	0.0318
NCMgOH5	10.7	1.0 M	0.8993	0.0693	0.0314
NCMgOH6	10.7	1.3 M	0.8894	0.0690	0.0416

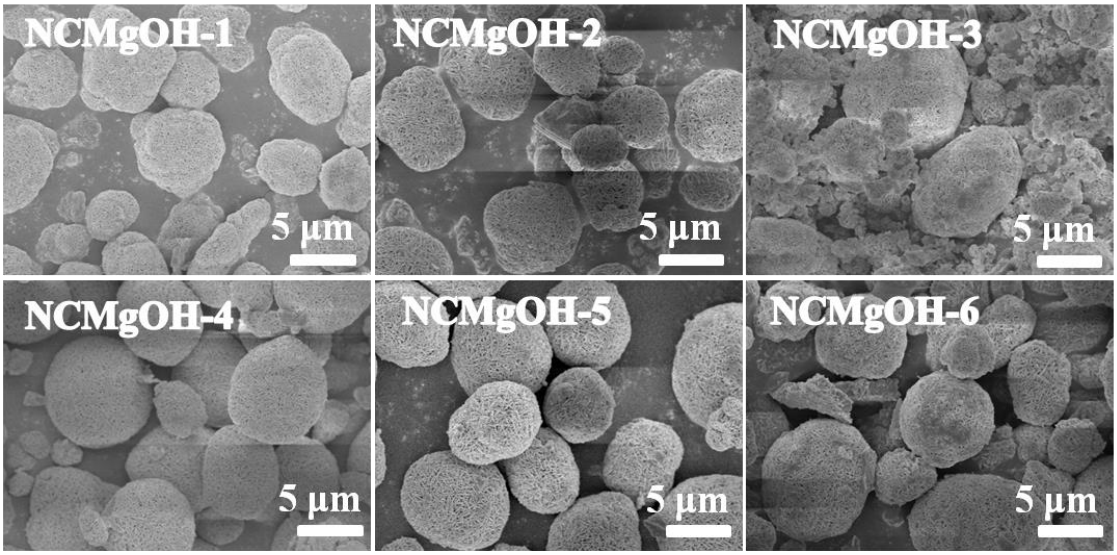

Figure S2. SEM images of (a) NCMgOH-1, (b) NCMgOH-2, (c) NCMgOH-3, (d) NCMgOH-4, (e) NCMgOH-5, and (f) NCMgOH-6 precursors.

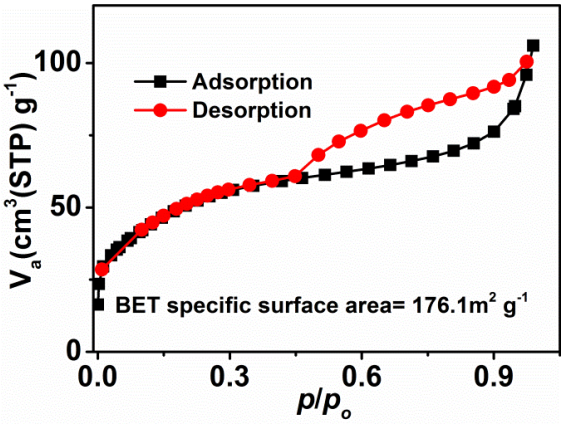

Figure S3. N_2 adsorption and desorption isotherms of $Ni_{0.9}Co_{0.07}Mg_{0.03}(OH)_2$ precursor. The hysteresis loop reflects porous structure.

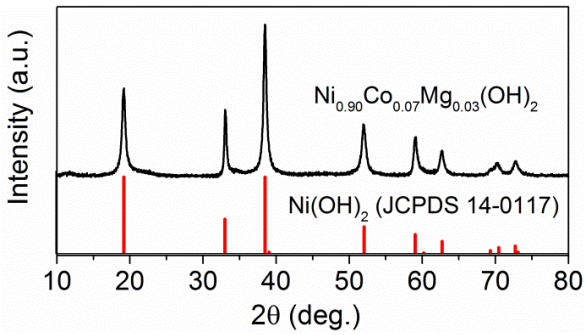

Figure S4. XRD pattern of $Ni_{0.9}Co_{0.07}Mg_{0.03}(OH)_2$ precursor.

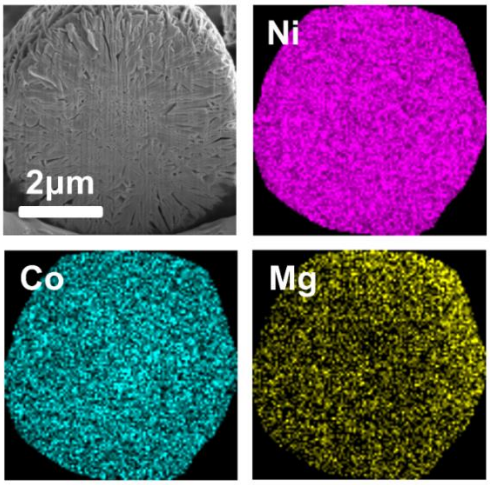

Figure S5. EDS elemental mapping of $Ni_{0.9}Co_{0.07}Mg_{0.03}(OH)_2$ precursor.

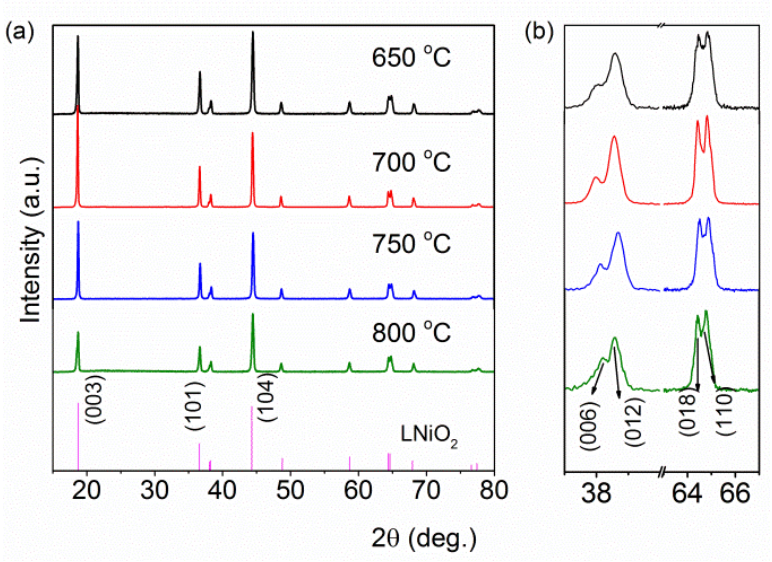

Figure S6. XRD patterns of $LiNi_{0.9}Co_{0.07}Mg_{0.03}O_2$ calcined at 650, 700, 750 and 800 °C.

Table S2. Structural parameters, $I_{(003)}/I_{(104)}$, and R-factor of $LiNi_{0.9}Co_{0.07}Mg_{0.03}O_2$ samples prepared at various calcination temperatures.

	650 °C	700 °C	750 °C	800 °C
a (Å)	2.871(8)	2.874(6)	2.870(5)	2.874(5)
c (Å)	14.174(3)	14.295(2)	14.191(4)	14.189(3)
c/a	4.937	4.974	4.945	4.937
I_{003}/I_{104}	0.943	1.343	1.162	0.711
R	0.508	0.474	0.528	0.738

The degree of the Ni^{2+}/Li^{+} mixing is measured by XRD analysis and the disordering leads to a decrease in intensity of the (003) peak and an increase in the (104) peak.[7] As a result, intensity ratio of (003)/(104) peaks is often used as a criterion to measure the degree of disordering. Moreover, we can evaluate the hexagonal ordering by calculating the R-factor, which equals to the value of [*I*(006)+ *I*(102)]/I(101). The smaller value of R-factor suggests better hexagonal ordering.[8] Finally, the splits of (006)/(012) and (018)/(110) indicate a well-developed layered structure.[9]

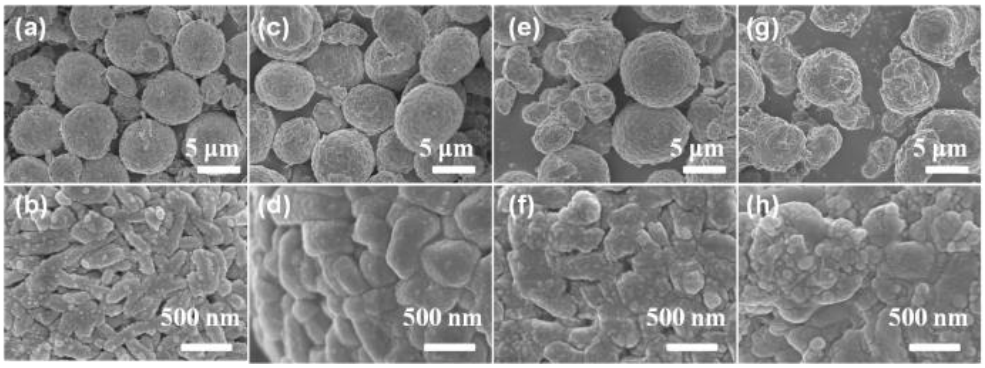

Figure S7. SEM of $LiNi_{0.9}Co_{0.07}Mg_{0.03}O_2$ calcined at (a,b) 650, (c,d) 700, (e,f) 750, and (g,h) 800 ^{o}C.

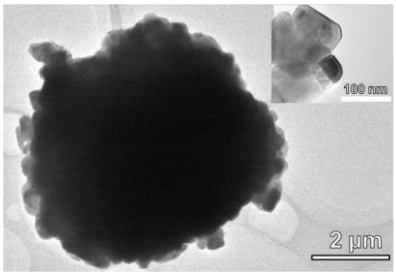

Figure S8. TEM images of $LiNi_{0.9}Co_{0.07}Mg_{0.03}O_2$. The inset shows the enlarged view from the edge of micro-sphere composed of cumulate primary particles.

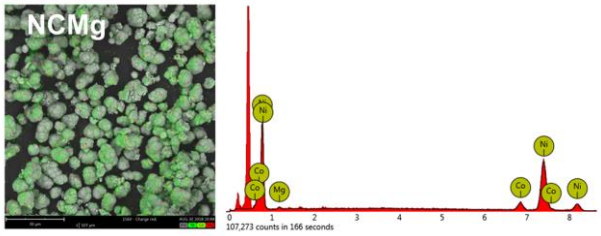

Figure S9. EDS elemental analysis of the synthesized $LiNi_{0.9}Co_{0.07}Mg_{0.03}O_2$ sample.

Table S3. Cationic distribution and lattice parameters of $LiNi_{0.9}Co_{0.07}Mg_{0.03}O_2$ determined from Rietveld refinement of XRD data.

Calculated Composition	**Lattice parameter**			***S*(MO$_2$)**	***I*(LiO$_2$)**	**R$_{wp}$**	**R$_B$**
	***a* (Å)**	***c* (Å)**	***Z$_{ox}$***	**(Å)**	**(Å)**	**(%)**	**(%)**
$(Li_{0.964}Mg_{0.021}Ni_{0.015})$ $(Ni_{0.881}Mg_{0.009}Li_{0.040}Co_{0.070})O_2$	2.873(5)	14.295(5)	0.259(2)	2.125	2.640	5.46	3.41

Z_{ox} is the position of O^{2-} along the *c* axis in a hexagonal cell. Typically, (0, 0, Z_{ox}) is used as the coordinate for O^{2-}. The slab thickness $S(MO_2)$ and the interslab thickness $I(LiO_2)$ correspond to the distances along the c_{hex} axis between the oxygen layers of the NiO_2 slab and LiO_2 interslab spaces, respectively. They are defined as $S(MO_2) = (2/3 – 2Z_{ox.})c_{hex.}$ and $I(LiO2) = (c_{hex}/3) - S(MO_2)$.[10] R_{wp} and R_B are the conventional Rietveld factors for points with Bragg contribution.

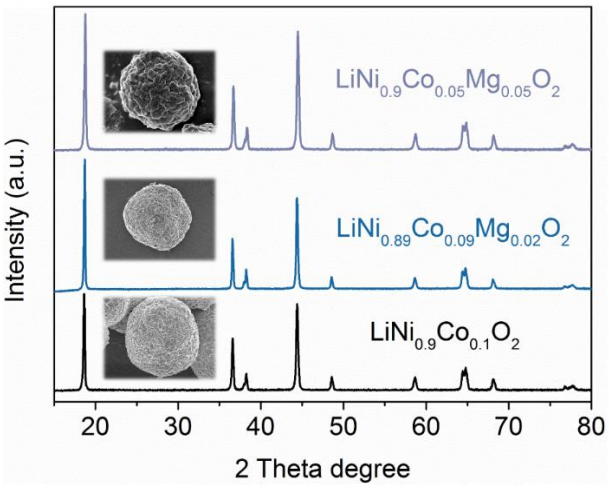

Figure S10. The XRD and corresponding SEM images of different Mg-doped samples.

Table S4. Structural parameters, $I_{(003)}/I_{(104)}$, and R-factor of different Mg-doped samples.

Composition	a	c	c/a	I_{003}/I_{104}	R
$LiNi_{0.90}Co_{0.10}O_2$	2.875	14.194	4.937	1.115	0.5788
$LiNi_{0.89}Co_{0.09}Mg_{0.02}O_2$	2.874	14.191	4.938	1.353	0.5088
$LiNi_{0.90}Co_{0.05}Mg_{0.05}O_2$	2.875	14.201	4.939	1.143	0.5487

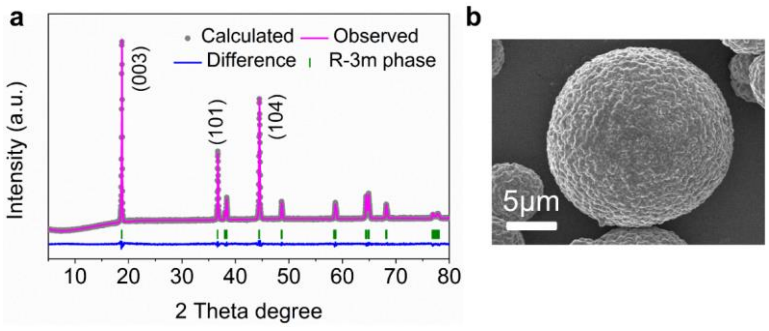

Figure S11. (a) Rietveld refined XRD pattern and (b) SEM image of commercial $LiNi_{0.8}Co_{0.1}Mn_{0.1}O_2$.

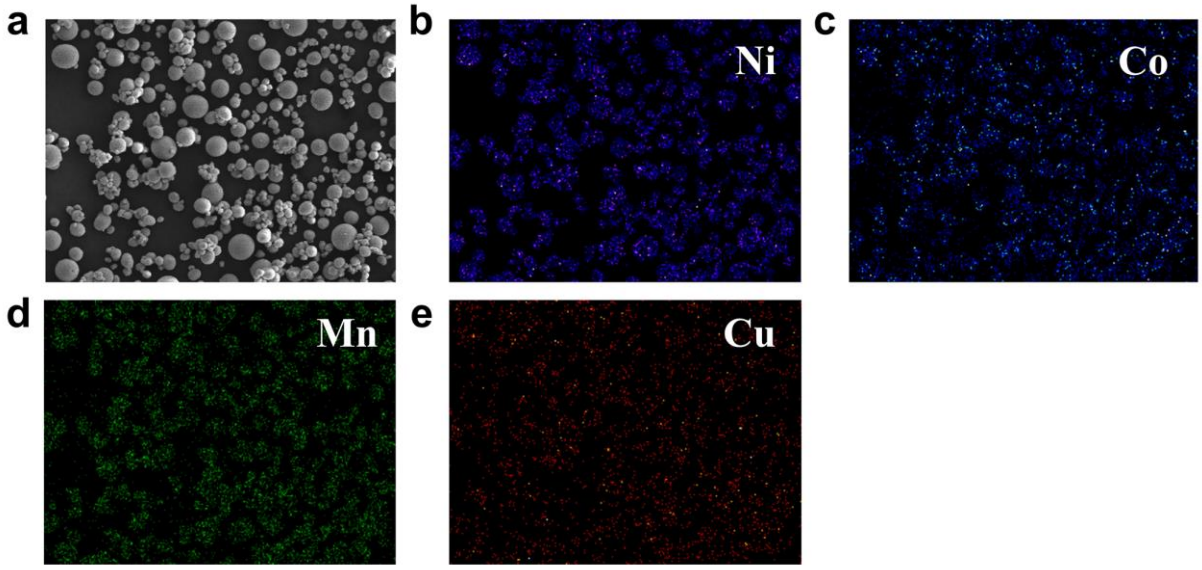

Figure S12. EDS element mapping of commercial $LiNi_{0.8}Co_{0.1}Mn_{0.1}O_2$ (NCM811). A small amount of Cu is detected, which arises from material modification by the supplier.

Table S5. Cationic distribution and lattice parameters of $LiNi_{0.8}Co_{0.1}Mn_{0.1}O_2$ (NCM811) determined by Rietveld refinement of XRD data.

Calculated Composition	**Lattice parameter**			***S*(MO$_2$)[a]**	***I*(LiO$_2$)[b]**	**R_{wp}**	**R_B**
	***a* (Å)**	***c* (Å)**	**$z_{ox.}$**	**(Å)**	**(Å)**	**(%)**	**(%)**
$(Li_{0.98}Ni_{0.02})$ $(Ni_{0.78}Li_{0.02}Co_{0.1}Mn_{0.1})O_2$	2.874(2)	14.216(5)	0.209(4)	3.524	1.215	1.9	1.44

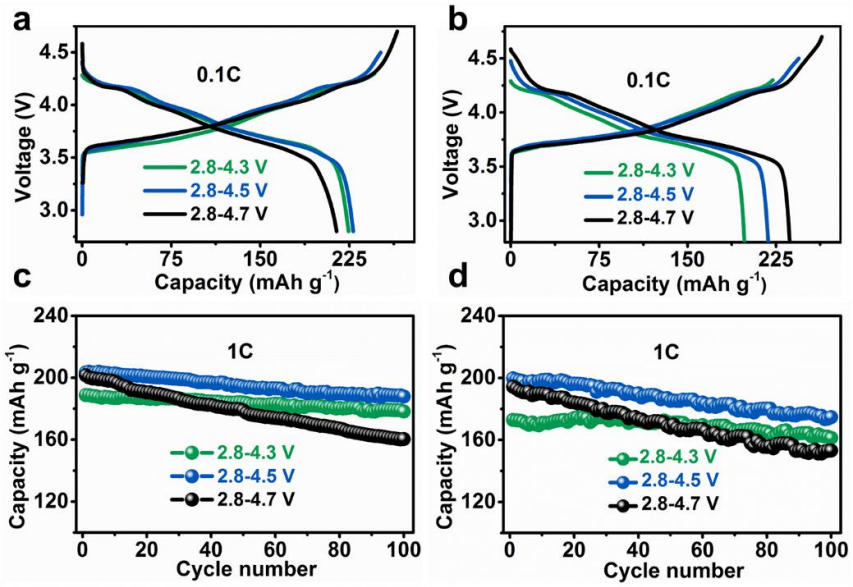

Figure S13. Initial charge/discharge curves (a,b) and cycling performance (c,d) of $LiNi_{0.9}Co_{0.07}Mg_{0.03}O_2$ (a,c) and NCM811 (b,d) within different voltage ranges.

Table S6. First-cycle electrochemical properties of NCMg within different voltage ranges at 0.1 C.

Charging voltage (V)	Charge capacity (mAh g^{-1})	Discharge capacity (mAh g^{-1})	Coulombic efficiency (%)
4.3	246.3	224.4	91.1
4.5	251.4	228.3	90.8
4.7	265.4	214.3	80.7

Table S7. First-cycle electrochemical properties of NCM811 within different voltage ranges at 0.1 C.

Charging voltage (V)	Charge capacity (mAh g^{-1})	Discharge capacity (mAh g^{-1})	Coulombic efficiency (%)
4.3	222.3	198.2	89.2
4.5	244.3	218.4	89.4
4.7	263.9	236.7	89.7

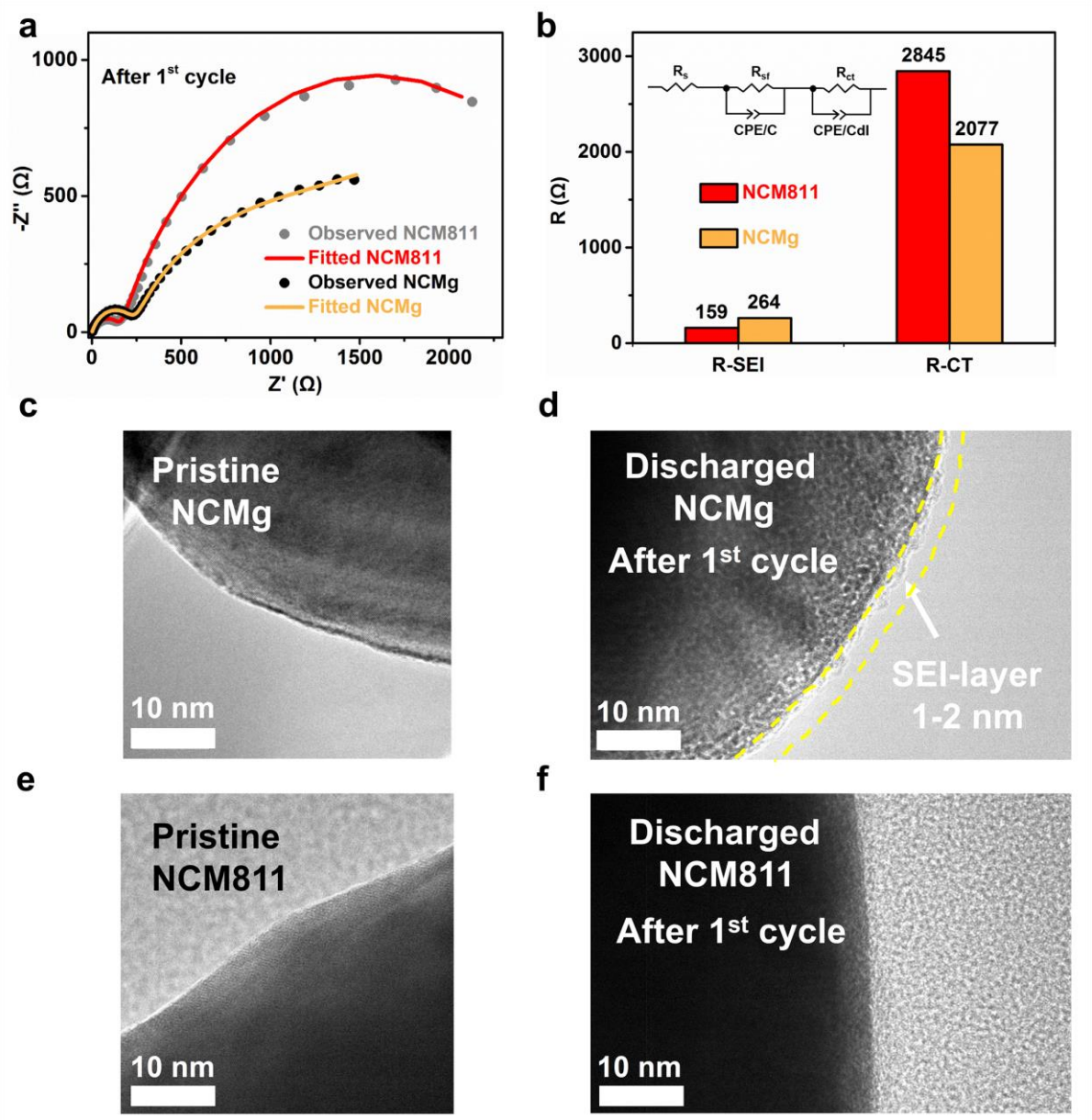

Figure S14. (a) Nyquist plots and fitted curves of discharged NCMg and NCM811 after one cycle within 2.8–4.7 V. (b) Fitted EIS results and equivalent circuit. (c-f) TEM images of NCMg and NCM811 electrodes at pristine state and at discharged state after one cycle within 2.8–4.7 V.

As expected, the charging capacity increases with charging voltages for both NCM811 and NCMg cathodes (Table S6,S7). However, the NCMg electrode shows a decrease of discharge capacity and Coulombic efficiency within 2.8–4.7 V. For NCM811, the initial Coulombic efficiency stabilizes above 89% and the discharge capacity increases from 198.2 to 236.7 mAh g^{-1} when the ending charge voltage is elevated from 4.3 to 4.7 V. Such different trend in discharge capacity could

be ascribed to the different degree of electrode/electrolyte side reaction, as suggested from the EIS results (Fig. S14a,b) that NCMg has a lower solid electrolyte interphase (SEI) impedance than NCM811. TEM imaging on pristine and discharged electrodes further evidences thicker SEI film on NCMg as compared to NCM811 (Fig. S14c-f). The more severe side reaction accounts for lower Coulombic efficiency within 2.8–4.7 V. The higher interface stability of commercial NCM811 possibly originates from material modification by suppliers (as deduced from the presence of Cu in EDS mapping, Figure S12).

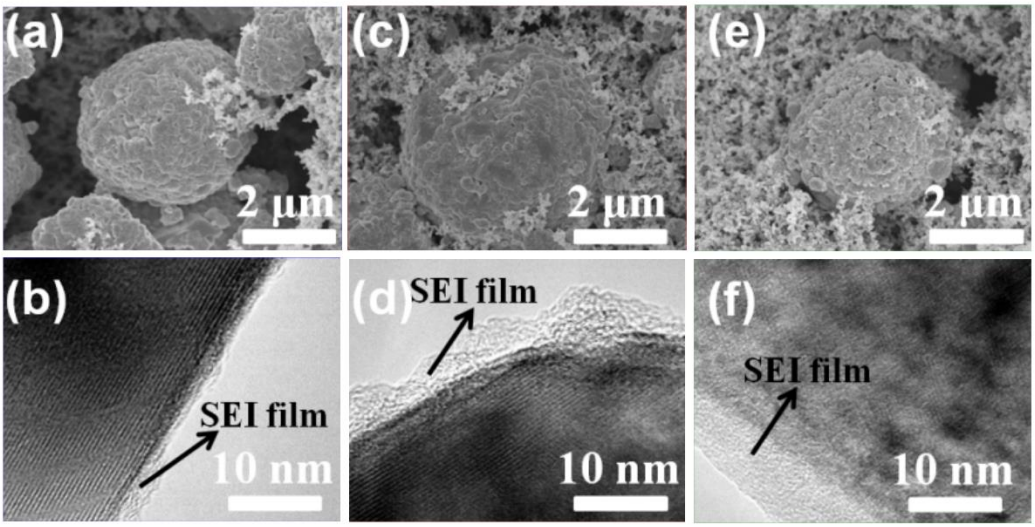

Figure S15. SEM and TEM images of $LiNi_{0.9}Co_{0.07}Mg_{0.03}O_2$ after 100 cycles at 1 C in the voltage range of (a, b) 2.8-4.3 V, (b, d) 2.8-4.5 V, (c, f) 2.8-4.7 V.

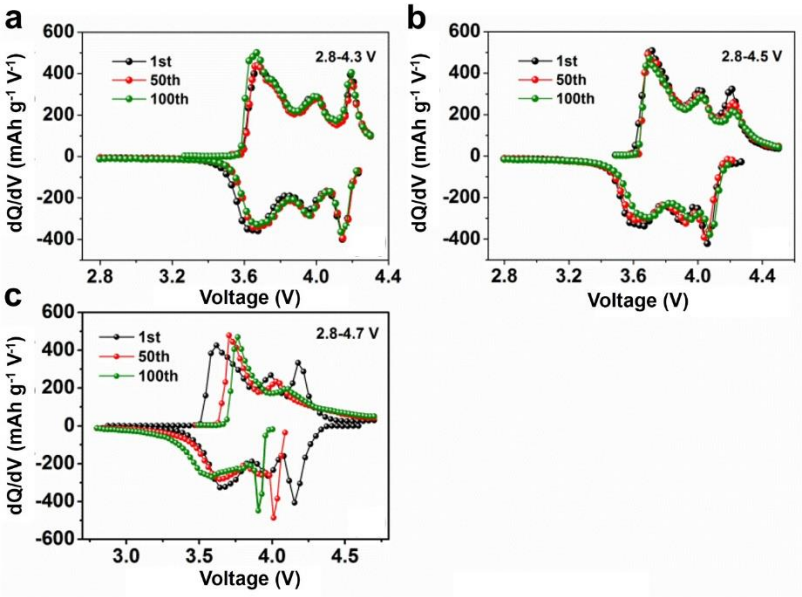

Figure S16. dQ/dV curves of different numbers of cycles at 1C for $LiNi_{0.9}Co_{0.07}Mg_{0.03}O_2$ in the voltage range of (a) 2.8-4.3 V, (b) 2.8-4.5 V, (c) 2.8-4.7 V.

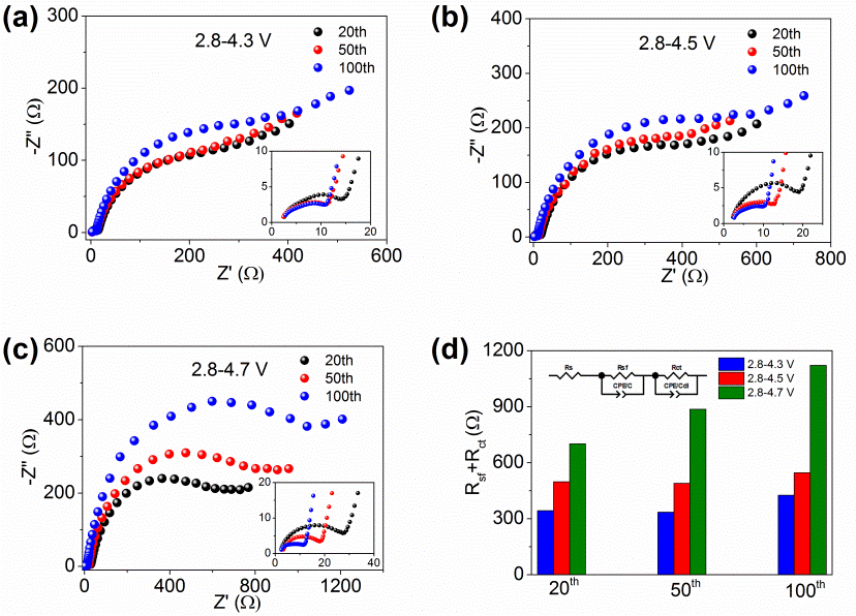

Figure S17. Nyquist plots of different numbers of cycles at 1 C for $LiNi_{0.9}Co_{0.07}Mg_{0.03}O_2$ in the voltage range of (a) 2.8-4.3 V, (b) 2.8-4.5 V, and (c) 2.8-4.7 V. (d) The fitting results of impedance based on the simplified equivalent circuit (inset).

The morphological change of $LiNi_{0.9}Co_{0.07}Mg_{0.03}O_2$ was further investigated by SEM and TEM after cycling within different voltage ranges (Fig. S15). For the electrodes after charging to 4.7 V, the

surface of microspheres became rough and more edges of the particles broke into small fragments, which was induced by the attack of HF and the dissolution of transition metal in the electrolyte.[12] Raising the charging voltage aggravates the side reactions and the resulting fragments provide new sites for electrode/electrolyte interface reactions, promoting the formation of dense and thick solid electrolyte interface (SEI) layers.[13] The thick SEI layer would retard Li^+ diffusion, increase interface impedance, and thus deteriorate the performance.[14] At elevated charged voltage, higher electrode polarization and larger charge transfer resistance were clearly seen from the differential capacity-voltage (dQ/dV) curves (Fig. S16) and EIS analysis (Fig. S17). Based on the above results, the $LiNi_{0.9}Co_{0.07}Mg_{0.03}O_2$ electrode was cycled within 2.8–4.5 V to achieve a balanced capacity and stability.

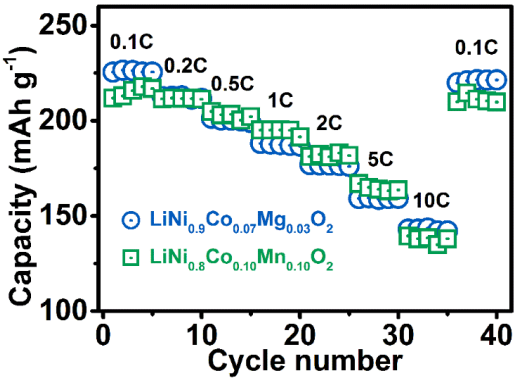

Figure S18. Rate capability of $LiNi_{0.9}Co_{0.07}Mg_{0.03}O_2$ and NCM811. The rate was gradually increased from 0.1 C to 10 C with each rate staying for five cycles. At 10 C, $LiNi_{0.9}Co_{0.07}Mg_{0.03}O_2$ delivers a high capacity of 142.8 mAh g^{-1}, which slightly exceeds that of NCM811 (137.8 mAh g^{-1}).

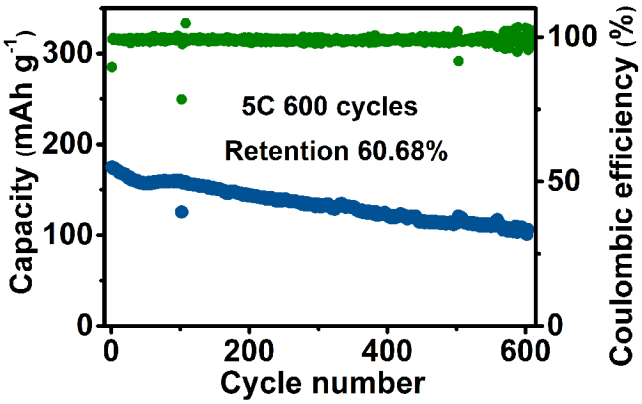

Figure S19. Extended cycling performance of $LiNi_{0.9}Co_{0.07}Mg_{0.03}O_2$ electrode at 5 C in the voltage range of 2.8-4.5 V.

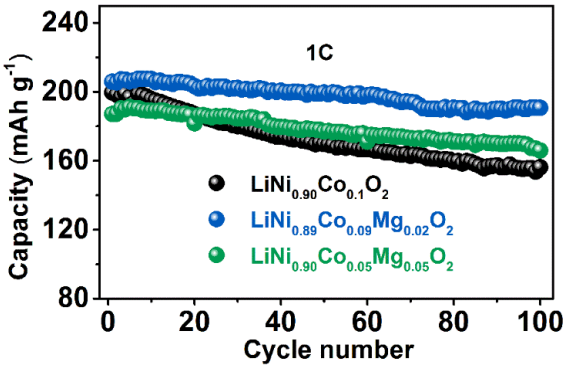

Figure S20. Cycling performance at 1 C in the voltage range of 2.8-4.5 V of different Mg compositions.

Table S8. Comparison of electrochemical performance of the cathodes with different Mg compositions.

Material	Voltage Window	Current Density (1 C = 180 mA g^{-1})	Initial Discharge capacity (mAh g^{-1})	Cycle Number	Initial Coulombic Efficiency (%)	Retention (%)
$LiNi_{0.90}Co_{0.10}O_2$	2.8-4.5V	1 C	199.6	100	87.04	78.26
$LiNi_{0.89}Co_{0.09}Mg_{0.02}O_2$	2.8-4.5V	1 C	205.9	100	82.46	92.62
$LiNi_{0.90}Co_{0.05}Mg_{0.05}O_2$	2.8-4.5V	1 C	187.4	100	83.92	88.72

Table S9. Comparison of cycling performance and rate capability for Ni-rich cathode materials.

Composition	1st discharge Capacity at 0.1 C (mAh g^{-1})	Cycling capacity at 25 °C (mAh g^{-1})				Rate capacity (C, mAh g^{-1})			Ref.
		Current density (mA g^{-1})	Cycle number	Reversible capacity	Capacity retention	1	5	10	
$LiNi_{0.80}Co_{0.15}Al_{0.05}O_2$	218	180	100	168	93%	172	137	115	15a
$LiNi_{0.81}Co_{0.10}Al_{0.09}O_2$	199	200	200	147.9	85%	176	161	155	9
$LiNi_{0.90}Co_{0.05}Mn_{0.05}O_2$	238	120	100	182	87%	193	165	N/A	15b
$LiNi_{0.80}Co_{0.01}Mn_{0.01}O_2$	201.4	200	100	168.2	90.6%	186	164	146	15c
$LiNi_{0.80}Co_{0.10}Mn_{0.10}O_2$	203	100	100	153	70.2%	N/A	N/A	N/A	15d
$LiCoO_2$	190	180	50	177	96%	174	N/A	N/A	15e
$LiNi_{0.65}Co_{0.13}Mn_{0.22}O_2$	200	100	100	182	96.6%	187	N/A	N/A	15f
$LiNi_{0.90}Co_{0.07}Al_{0.03}O_2$	236	180	100	179.8	93.1%	193	168	140	15g
$LiNi_{0.90}Co_{0.07}Mg_{0.03}O_2$	251.3	180	100	189	92.2%	187	159	143	This work

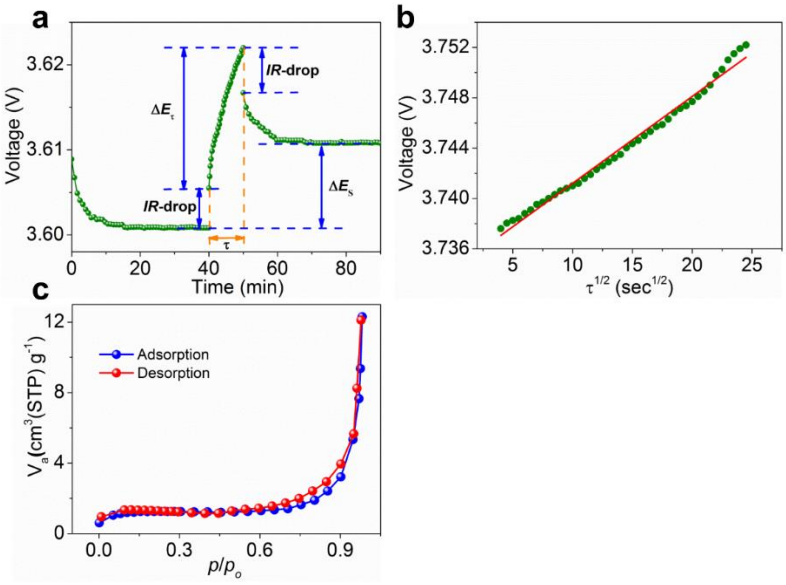

Figure S21. (a) The diagram for the voltage response of a charge pulse at around 3.61 V in the GITT experiment with the labelling of parameters. (b) The plot of voltage against $\tau^{1/2}$ and the linear fitting. (c) N_2 adsorption and desorption isotherms of the composite electrode. The BET surface area of the

composite electrode (3.28 m^2 g^{-1}) is used as the total contact area rather than the geometric area of the electrode (0.785 cm^2).

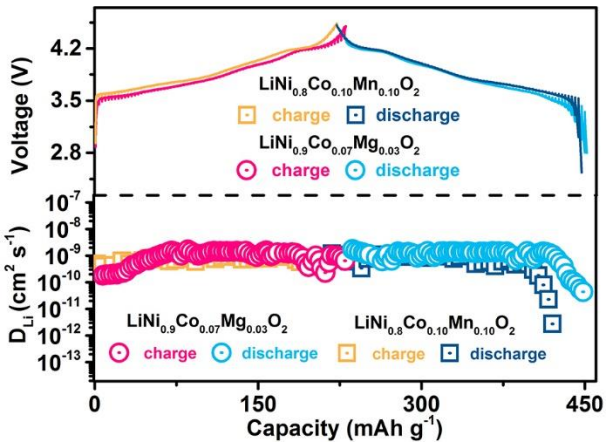

Figure S22. GITT curves and calculated D_{Li^+} in the voltage range of 2.8–4.5 V. The determined D_{Li^+} values of $LiNi_{0.9}Co_{0.07}Mg_{0.03}O_2$ vary from 4.37 × 10^{-11} to 1.51 × 10^{-9} cm^2 s^{-1}, with an average value of 9.64 × 10^{-10} and 1.07 × 10^{-9} cm^2 s^{-1} for the charge and discharge process, respectively.

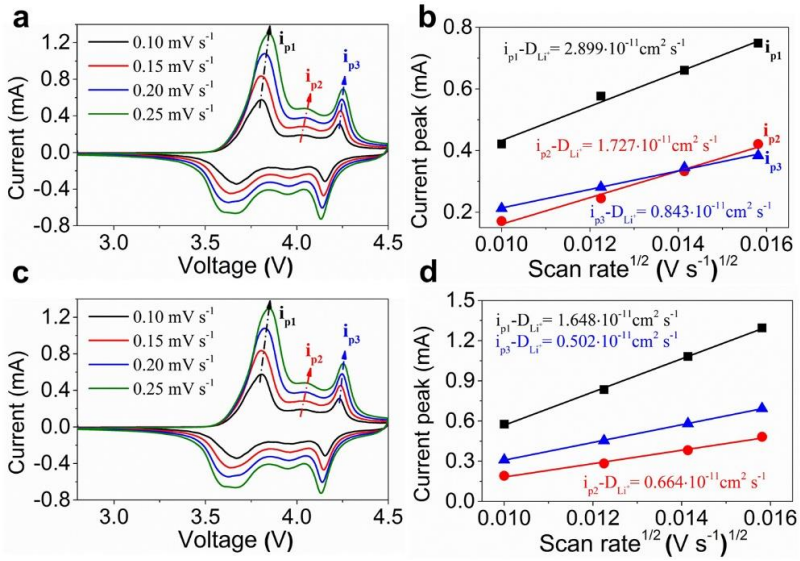

Figure S23. CVs at various scanning rates (a,c) and linear relationship between the peak currents and scan rates (b,d) for $LiNi_{0.9}Co_{0.07}Mg_{0.03}O_2$ (a,b) and $LiNi_{0.8}Co_{0.1}Mn_{0.1}O_2$ (c,d). D_{Li^+} is calculated by the equation $i_p = (2.69\times10^5)n^{3/2}AD_{Li^+}^{1/2}C_{Li}^{*}v^{1/2}$, where i_p, n and C_{Li} are peak current, charge transfer number, and concentration of Li^+ in the active material, respectively.[16] The value of D_{Li^+} at

each oxidation peak position for NCM811 is lower than that of $LiNi_{0.9}Co_{0.07}Mg_{0.03}O_2$, which is consistent with the GITT results.

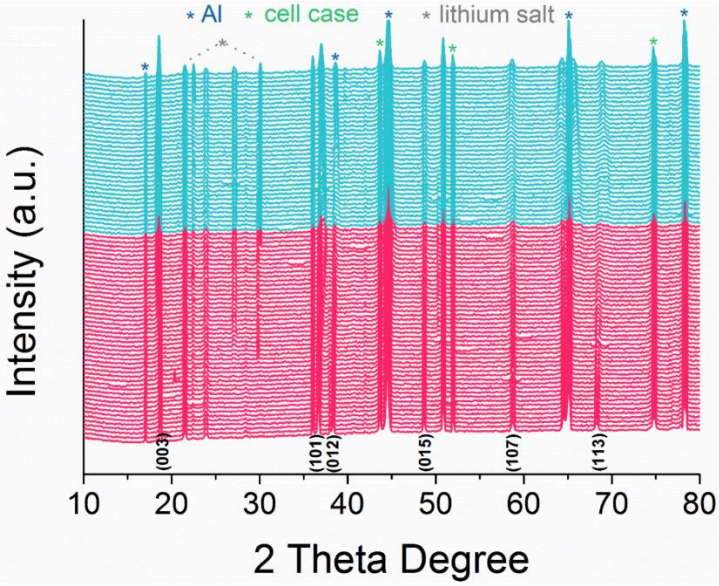

Figure S24. *In-situ* XRD patterns of $LiNi_{0.9}Co_{0.07}Mg_{0.03}O_2$ cathode during the first cycling process at a 0.2 C rate in the voltage range of 2.8–4.7 V.

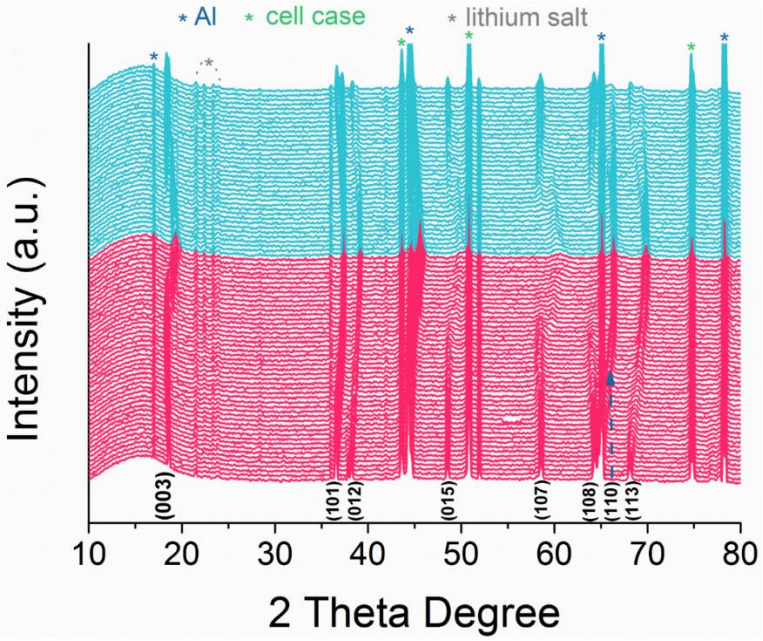

Figure S25. *In-situ* XRD patterns of $LiNi_{0.8}Co_{0.1}Mn_{0.1}O_2$ (NCM811) cathode during the first cycling process at a 0.2 C rate in the voltage range of 2.8–4.7 V.

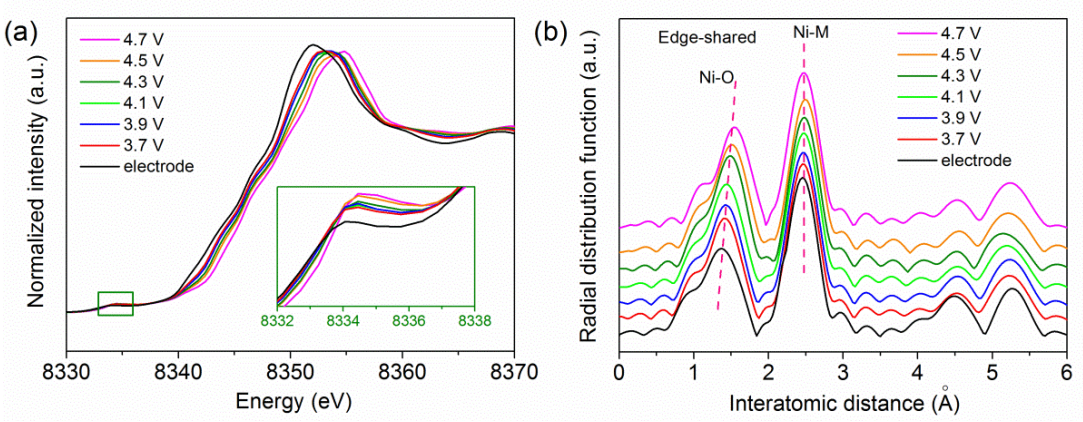

Figure S26. Ex suit XAS of the $LiNi_{0.9}Co_{0.07}Mg_{0.03}O_2$ cathode during the first charge at 0.1 C: (a) Ni K-edge XANES spectra, (b) Ni K-edge Fourier transform magnitudes of k3 weighted EXAFS spectra.

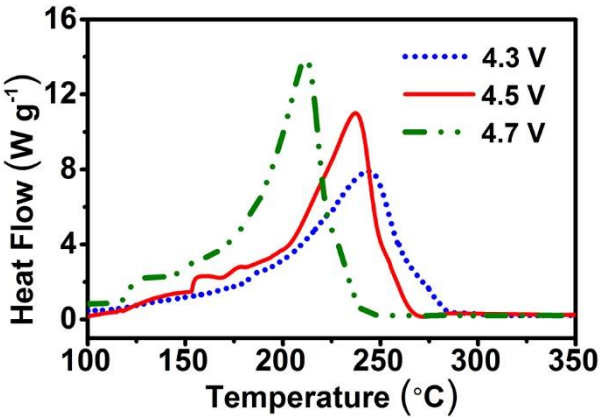

Figure S27. DSC profiles of the delithiated $Li_xNi_{0.9}Co_{0.07}Mg_{0.03}O_2$ charged to 4.3, 4.5, and 4.7 V.

Table S10. Comparison of the thermal stability of Ni-based cathode materials.

Materials	Charged voltage	Peak temperature	Heat generation	Ref.
$Li_{0.37}Ni_{1/3}Co_{1/3}Mn_{1/3}O_2$	4.3 V	306 °C	512.5 J/g	15d
$Li_{0.3}Ni_{0.6}Co_{0.2}Mn_{0.2}O_2$	4.3 V	264 °C	721.4 J/g	15d
$Li_{0.26}Ni_{0.7}Co_{0.15}Mn_{0.15}O_2$	4.3 V	242 °C	826.3 J/g	15d
$Li_{0.23}Ni_{0.8}Co_{0.1}Mn_{0.1}O_2$	4.3 V	232 °C	904.8 J/g	15d
$Li_{0.21}Ni_{0.85}Co_{0.075}Mn_{0.075}O_2$	4.3 V	225 °C	971.5 J/g	15d

$Li_xNi_{0.75}Co_{0.1}Mn_{0.15}O_2$	4.3 V	257.3 °C	718.1 J/g	17
$Li_xNi_{0.8}Co_{0.1}Mn_{0.1}O_2$	4.5 V	220.9 °C	720.8 J/g	15e
$Li_xNi_{0.9}Co_{0.05}Mn_{0.05}O_2$	4.3 V	201 °C	1670 J/g	15b
$Li_xNi_{0.81}Co_{0.10}Al_{0.09}O_2$	4.5 V	231 °C	466 J/g	9
$Li_xNi_{0.9}Co_{0.07}Al_{0.03}O_2$	4.3 V	221 °C	517.5 J/g	15g
$Li_xNi_{0.9}Co_{0.07}Mg_{0.03}O_2$	4.3 V	243.7 °C	543.2 J/g	This work
	4.5 V	242.6 °C	596.8 J/g	
	4.7 V	220.4 °C	667.5 J/g	

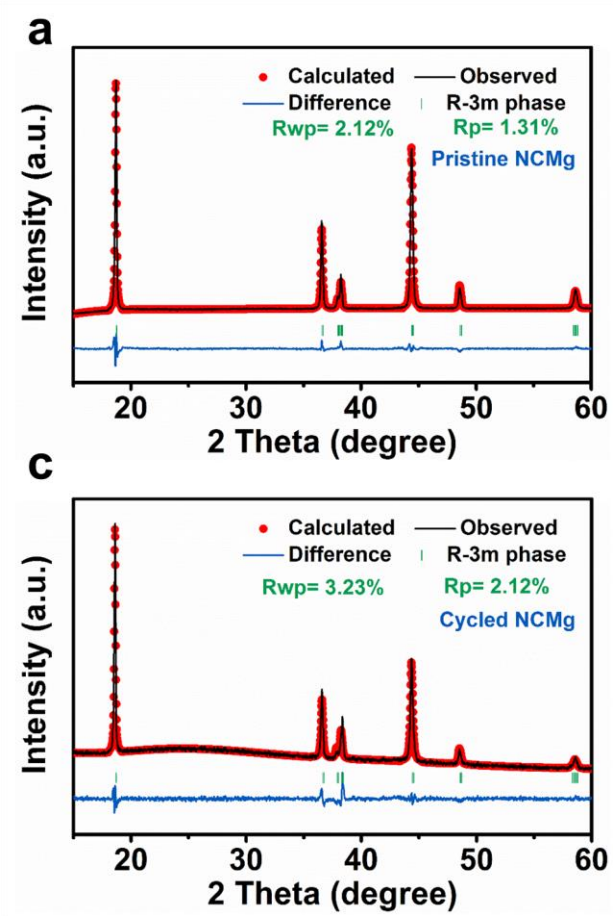

b

Site	x	y	z	Occupancy
Li1	0.0000	0.0000	0.0000	0.970(7)
Ni1	0.0000	0.0000	0.0000	0.019(5)
Mg1	0.0000	0.0000	0.0000	0.010(7)
Li2	0.0000	0.0000	0.5000	0.029(4)
Ni2	0.0000	0.0000	0.5000	0.878(3)
Mg2	0.0000	0.0000	0.5000	0.009(4)
Co1	0.0000	0.0000	0.5000	0.095(0)
O1	0.0000	0.0000	0.255(4)	1.000(0)
Li/Ni cation mixing (Ni^{2+} in Li sites) = 1.95%				

d

Site	x	y	z	Occupancy
Li1	0.0000	0.0000	0.0000	0.969(6)
Ni1	0.0000	0.0000	0.0000	0.020(0)
Mg1	0.0000	0.0000	0.0000	0.010(4)
Li2	0.0000	0.0000	0.5000	0.025(0)
Ni2	0.0000	0.0000	0.5000	0.870(0)
Mg2	0.0000	0.0000	0.5000	0.009(6)
Co1	0.0000	0.0000	0.5000	0.082(7)
O1	0.0000	0.0000	0.253(9)	1.000(0)
Li/Ni cation mixing (Ni^{2+} in Li sites) = 2.0%				

Figure S28. Rietveld refinement data of Mg-doped Ni-rich (NCMg) cathode (a,b) before and (c,d) after cycling at 2 C for 100 cycles. The XRD data ranging from 2Theta degree of 60–80 ° were not used in the refinement process to avoid the interference of reflection from Al current collector.

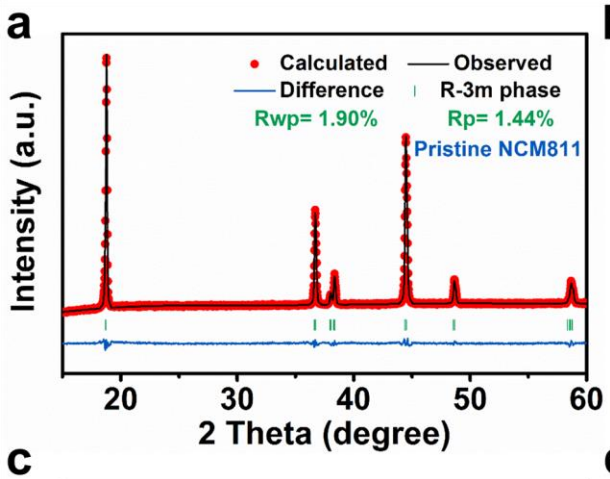

b

Site	x	y	z	Occupancy
Li1	0.0000	0.0000	0.0000	0.980(0)
Ni1	0.0000	0.0000	0.0000	0.020(0)
Li2	0.0000	0.0000	0.5000	0.020(0)
Ni2	0.0000	0.0000	0.5000	0.780(0)
Co1	0.0000	0.0000	0.5000	0.100(0)
Mn1	0.0000	0.0000	0.5000	0.100(0)
O1	0.0000	0.0000	0.209(1)	1.000(0)
Li/Ni cation mixing (Ni^{2+} in Lisites) = 2.0%				

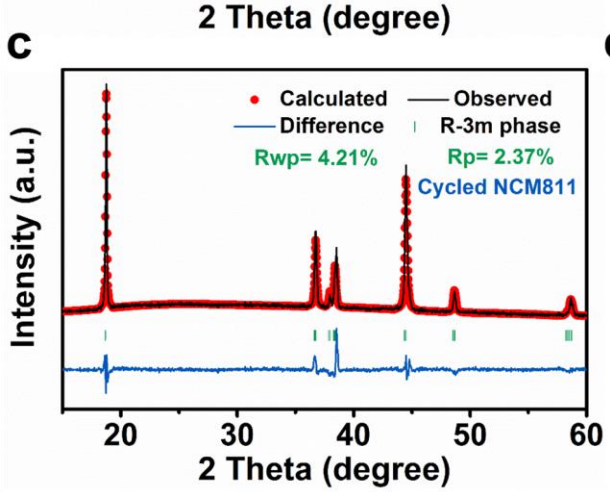

d

Site	x	y	z	Occupancy
Li1	0.0000	0.0000	0.0000	0.955(6)
Ni1	0.0000	0.0000	0.0000	0.034(4)
Li2	0.0000	0.0000	0.5000	0.031(6)
Ni2	0.0000	0.0000	0.5000	0.768(4)
Co1	0.0000	0.0000	0.5000	0.100(2)
Mn1	0.0000	0.0000	0.5000	0.096(2)
O1	0.0000	0.0000	0.256(1)	1.000(0)
Li/Ni cation mixing (Ni^{2+} in Li sites) = 3.4%				

Figure S29. Rietveld refinement data of NCM811 cathode (a,b) before and (c,d) after cycling at 2 C for 100 cycles. The XRD data ranging from 2Theta degree of 60–80 °were not used in the refinement process to avoid the interference of reflection from Al current collector.

References

1. C. Pouillerie, L. Croguennec, P. Biensan, P. Willmann, C. Delmas, *J. Electrochem. Soc*. 2000, **147**, 2061-2069.
2. S. D. Findlay, N. Shibata, H. Sawada, E. Okunishi, Y. Kondo, Y. Ikuhara, *Ultramicroscopy* 2010, **110**, 903-923.
3. R. Huang, Y. H. Ikuhara, T. Mizoguchi, S. D. Findlay, A. Kuwabara, C. A. J. Fisher, H. Moriwake, H. Oki, T. Hirayama, Y. Ikuhara, *Angew. Chem. Int. Ed.* 2009, **464,** 3053-3057.
4. R. Huang, T. Hitosugi, S. D. Findlay, C. A. J. Fisher, Y. H. Ikuhara, H. Moriwake, H. Oki, Y. Ikuhara, *Appl. Phys. Lett.* 2011, 98, 051913.

5. X. Lu, L. Zhao, X. Q. He, R. J. Xiao, L. Gu, Y. S. Hu, H. Li, Z. X. Wang, X. F. Duan, L. Q. Chen, J. Maier, Y. Ikuhara, *Adv. Mater.* 2012, **24**, 3233-3238.

6. a) X. H. Rui, N. Yesibolati, S. R. Li, C. C. Yuan, C. C. Chen, *Solid State Ionics* 2011, **187**, 58-63; b) J. Xie, K. Kohno, T. Matsumura, N. Imanishi, A. Hirano, Y. Takeda, O. Yamamoto, *Electrochim. Acta* 2008, **54**, 376-381.

7. J. R. Dahn, U. V. Sacken, C. A. Michal, *Solid State Ionics* 1990, **44**, 87-97.

8. X. Y. Zhang, A. Mauger, Q. Lu, H. Groult, L. Perrigaud, F. Gendron, C. M. Julien, *Electrochim. Acta* 2010, **55**, 6440-6449.

9. M. Jo, M. Noh, P. Oh, Y. Kim, J. Cho, *Adv. Energy Mater*. 2014, **4**, 1301583.

10. C. Pouillerie, F. Perton, P. Biensan, J. P. Peres, M. Broussely, C. Delmas, *J. Power Sources* 2001, **96**, 293-302.

11. a) G. Cherkashinin, M. Motzko, N. Schulz, T. Spath, W. Jaegermann, *Chem. Mater*. 2015, **27**, 2875-2887; b) L. E. Downie, S. R. Hyatt, J. R. Dahn, *J. Electrochem. Soc.* 2016, **163**, A35-A42.

12. a) K. Edstrom, T. Gustafsson, J. O. Thomas, *Electrochim. Acta* 2004, **50**, 337-364; b) D. Aurbach, *J. Power Source* 2000, **89**, 206-218.

13. a) J. A. Gilbert, I. A. Shkrob, D. P. Abraham, *J. Electrochem. Soc.* 2017, **164**, A389-A399; b) A. M. Andersson, D. P. Abraham, R. Haasch, S. Maclaren, J. Liu, K. Amine, *J. Electrochem. Soc*. 2002, **149**, A1358-A1369.

14. C. H. Chen, J. Liu, K. Amine, *J. Power Source* 2001, **96**, 321-328.

15. a) N. T. Wu, H. Wu, Y. Wei, S. J. Liu, J. Y. Liao, Y. Zhang, *J. Mater. Chem. A* 2015, **3**, 13648-13652; b) H. H. Sun, A. Manthiram, *Chem. Mater.* 2017, **29**, 8486-8493; c) J. M. Zheng, W. H. Kan, A. Manthiram, *ACS Appl. Mater. Interfaces.* 2015, **7**, 6926-6934; d) H.-J. Noh, S. Youn, C. S. Yoon, Y.-K. Sun, *J. Power Sources* 2013, **233**, 121-130; e) Q. Liu, X. Su, D. Lei, Y. Qin, J. G. Wen, F. M. Guo, Y. A. Wu, Y. C. Rong, R. H. Kou, X. H. Xiao, F. Aguesse, J. Bareno, Y. Ren, W. Q. Lu, Y. X. Li, *Nat. Energy* 2018, **3**, 936-943; f) B.-B. Lim, S.-J. Yoon, K.-J. Park, C. S. Yoon, S.-J. Kim, J. J. Lee, Y.-K. Sun, *Adv. Funct. Mater*. 2015, **25**, 4673-4680; g) P. F. Zhou, H. J. Meng, Z. Zhang, C. C. Chen, Y. Y. Lu, J. Cao, F. Y. Cheng, J. Chen, *J. Mater. Chem. A* 2017, **5**, 2724-2731.

16. C. C. Chen, Y. N. Huang, C. H. An, H. Zhang, Y. J. Wang, L. F. Jiao, H. T. Yuan, *ChemSusChem* 2015, **8**, 114-122.

17. Y.-K. Sun, Z. H. Chen, H. J. Noh, D.-J. Lee, H.-G. Jung, Y. Ren, S. Wang, C. S. Yoon, S.-T. Myung, K. Amine, *Nat. Mater*. 2012, **11**, 942.